

On the comparison of AGN with GRMHD simulations: I. Sgr A*

Richard Anantua^{1,2,3}   Sean Ressler^{1,4,5} and Eliot Quataert^{1,4} 

¹*Astronomy Department, Theoretical Astrophysics Center, University of California, Berkeley, 601 Campbell Hall, Berkeley, CA 94720, USA*

²*Center for Astrophysics | Harvard & Smithsonian, 60 Garden Street, Cambridge, MA 02138, USA*

³*Black Hole Initiative at Harvard University, 20 Garden Street, Cambridge, MA 02138, USA*

⁴*Department of Physics, University of California Berkeley, 1 LeConte Hall, Berkeley, CA 94720, USA*

⁵*Kavli Institute for Theoretical Physics, University of California Santa Barbara, Kohn Hall, Santa Barbara, CA 93107, USA*

Accepted 2020 January 29. Received 2020 January 27; in original form 2019 May 18

ABSTRACT

We present models of Galactic Centre emission in the vicinity of Sagittarius A* that use parametrizations of the electron temperature or energy density. These models include those inspired by two-temperature general relativistic magnetohydrodynamic (GRMHD) simulations as well as jet-motivated prescriptions generalizing equipartition of particle and magnetic energies. From these models, we calculate spectra and images and classify them according to their distinct observational features. Some models produce morphological and spectral features, e.g. image sizes, the sub-mm bump, and low-frequency spectral slope compatible with observations. Models with spectra consistent with observations produce the most compact images, with the most prominent, asymmetric photon rings. Limb-brightened outflows are also visible in many models. Of all the models we consider, that which represents the current data the best is one in which electrons are relativistically hot when magnetic pressure is larger than the thermal pressure, but cold (i.e. negligibly contributing to the emission) otherwise. This work is part of a series also applying the ‘observing’ simulations methodology to near-horizon regions of supermassive black holes in M87 and 3C 279.

Key words: black hole physics – accretion, accretion discs – MHD.

1 INTRODUCTION

Merely $d = 8.18$ kpc away (Abuter et al. 2019) at the Galactic Centre, Sagittarius A* (Sgr A*) is the best known accreting supermassive black hole. With $m_{\text{BH}} = 4.14$ million solar masses (Abuter et al. 2019) (subtending 5.0 μas at Earth), Sgr A* is a prime candidate for the next measurement of a black hole shadow by the Event Horizon Telescope (EHT; Doeleman et al. 2008) – after the one in the giant elliptical galaxy M87. In 2019 April, the EHT imaged emission around the central supermassive black hole of M87, finding a 42 μas -wide annulus with a Southern excess consistent with relativistic predictions of beamed emission in the Kerr metric of a 6.5 billion solar mass black hole (Event Horizon Telescope Collaboration et al. 2019). The distribution of flux density over the EHT M87 image – along with a conservative lower bound on the jet power of $L_{\text{M87}} \geq 10^{42} \text{ erg s}^{-1}$ – precludes models with a non-spinning black hole, supporting the interpretation of the M87 jets as powered by the Blandford–Znajek mechanism (Blandford & Znajek 1977). Image reconstruction of Sgr A* data has presented unique challenges relative to that for M87 due to the dynamical time-scales of minutes as opposed to days (Event Horizon Telescope

Collaboration et al. 2019). GRAVITY (Gillessen et al. 2010) has recently measured astrometrically the proper motion of several ‘hot spots’ (i.e. near-infrared flares) orbiting the Galactic Centre black hole at \sim 6–10 gravitational radii ($M \equiv r_{\text{g}} = Gm_{\text{BH}}/c^2$),¹ suggesting that the innermost accretion flow may be relatively face on and strongly magnetized (Gravity Collaboration et al. 2018). These horizon-scale probes of plasma physics, accretion physics, and strong general relativistic effects provide strong constraints on theoretical models.

Incorporating all these effects into analytic models is difficult, and thus general relativistic magnetohydrodynamic (GRMHD) simulations are the most promising avenues for theoretical modelling (Gammie, McKinney & Tóth 2003; Sadowski et al. 2014; White, Stone & Gammie 2016; Porth et al. 2017). These simulations solve the equations of MHD in the Kerr metric for a rotating black hole in 3+1 dimensions, naturally capturing the magnetorotational instability (MRI), the formation of jets, turbulence, and general relativistic effects.

As an especially low-luminosity active galactic nucleus (LLAGN) with an observed Eddington ratio $\sim 10^{-9}$ (Kataoka et al. 2018), the dynamical time for accretion in Sgr A* is much shorter

* E-mail: ranantua@cfa.harvard.edu

¹ M for Sgr A* corresponds to $6.08 \times 10^9 \text{ m}$, 20.25 s, and 4.96 μas .

than the electron-ion Coulomb collision time. This means that the flow can roughly be described as a two-temperature plasma (Mahadevan & Quataert 1997) and that information beyond that provided by the standard GRMHD equations is needed to constrain the electron temperature, a key parameter in emission modelling. Many approaches have been taken in the Literature for setting the electron temperature. Simple post-processing prescriptions that ‘paint on’ electron temperatures, such as those that set a constant electron-to-proton temperature ratio (Mościbrodzka et al. 2009) everywhere or that set the electron temperature to be some function of plasma parameters (Shcherbakov, Penna & McKinney 2012; Mościbrodzka & Falcke 2013; Chan et al. 2015), are useful for rapidly and directly connecting observations to model parameters. More sophisticated treatments directly evolve the electron temperature alongside the single-fluid equations of GRMHD and incorporate knowledge of electron/ion heating gained from particle-in-cell (PIC) simulations of collisionless plasmas (Ressler et al. 2015, 2017; Sadowski et al. 2017; Chael et al. 2018). Though these models are more physically motivated and self-consistent, they are more expensive to run which makes it difficult to fully explore the parameter space of electron temperature spanned by our uncertainty in the dominant mechanism of electron/ion heating. Furthermore, conservative GRMHD simulations are unable to properly model the thermodynamics of flows in which the magnetic energy density far exceeds the rest mass energy density (as it often does in the jet). Thus, two-temperature simulations that rely on an accurate calculation of the total fluid heating rate cannot be trusted in these regions; parametric models that depend only on the more reliable local magnetic energy density may be more appropriate there.²

Given this uncertainty, we consider it instructive to further explore the dependence of the spectra and near-horizon-scale images of Sgr A* on different post-processing models of the electron temperature. In doing so, we include not only some of the prescriptions used in past work to model the Galactic Centre, but also those attempting to mimic the qualitative behaviour seen in recent two-temperature GRMHD simulations and those successfully used to model other systems (e.g. Blandford & Königl 1979; Blandford & Anantua 2017; Anantua, Blandford & Tchekhovskoy 2018; Anantua, Emami & Loeb 2019). We synthesize our results by categorizing the synthetic images and spectra into a small number of groups according to their emission physics. This programme adds to the foundation of efforts at classifying and understanding jet (or outflow)/accretion disc/black hole (JAB) emission through a unified framework flexible enough to model disc, corona and outflow or jet regions with a small set of parameters – a methodology we call ‘Observing’ JAB Simulations.

This work is a small addition to a vast literature on post-processing simulations to understand JAB systems in the low accretion limit. For example, Dexter, Agol & Fragile (2009) simulated Sgr A* visibility amplitudes concordant with observed VLBI using 30 deg inclination angle from the black hole spin axis and generated synthetic light curves with 30 min rise times and up to 50 per cent

²This may be part of the reason why two-temperature GRMHD simulations of Sgr A* have thus far underproduced the low-frequency radio emission of Sgr A* (Ressler et al. 2017; Chael et al. 2018), as that emission is often assumed to be powered by the magnetized outflow. Alternatively, a small population of non-thermal particles can also explain the ~flat low-frequency radio spectrum (Özel, Psaltis & Narayan 2000; Yuan, Markoff & Falcke 2002).

flux modulation. Gold et al. (2017) compare synthetic Stokes maps of turbulent versus ordered magnetically arrested disc B -field configurations to EHT polarization data and favour the latter to account for the morphology and degree of linear polarization. GRMHD simulations in Mościbrodzka et al. (2014) explain the Sgr A* radio spectrum and image size primarily by efficient electron heating in the outflow plasma. Ryan et al. (2018) use general relativistic radiative magnetohydrodynamic (GRRMHD) simulations to model the M87 inner accretion flow and find inverse Compton cooling has a non-negligible back-reaction within $10M$. This work systematically considers simple parametric emission models to directly link microphysical processes to discrete observational signatures in Sgr A* and other AGN.

This paper is structured as follows. Section 2 is a brief synopsis of the observations of Sgr A* used to constrain our models; Section 3 describes the numerical simulations used in this work; Section 4 presents models for the accretion flow, electron temperature and emission; Section 5 provides results: images, spectra and light curves for our models; Section 6 compares the models in three different simulations to each other and to observations, resulting in a classification distilling various model morphologies, sizes and spectral shapes into four types; and Section 7 concludes.

In what follows, the speed of light, c , and the Boltzmann constant, k_B , are set to unity. Charge neutrality requires the electron number density, n_e , to be \approx the proton number density, $n_p \equiv n_0$. Then, the mass density is $\rho \approx \rho_p = m_p n_0$, where m_p is the mass of a proton. Setting m_p to 1 gives $P_e = \rho T_e$. The total temperature, $T_{\text{tot}} = T_e + T_p$, is given by the simulation; T_e is modelled.

2 OBSERVATIONS

Sgr A* has been observed for many years now in the radio, mm, infrared, and X-rays (Fish et al. 2011; Neilsen et al. 2013; Bower et al. 2015; Gravity Collaboration et al. 2018). Time variability tends to increase with frequency, with the radio emission being the most stable and the infrared and X-ray emission showing frequent occurrence of large amplitude flares, likely caused by non-thermal particle acceleration. Since we consider only thermal emission in this work, we treat the 10 per cent of the quiescent X-ray flux estimated to originate close to the black hole (Neilsen et al. 2013) as an upper limit. For a comprehensive list of the observational data points used in this work as constraints on our models (and plotted alongside our model spectra), see Ressler et al. (2017).

We use a 2D Gaussian semimajor axis size constraint of 49–63 μas (9.9–12.7 M) incorporating long baseline data (Johnson et al. 2015; Lu et al. 2018) in an elliptical ring interpretation of the image to constrain our model image size. At 3.5 mm (86 GHz), Issaoun et al. (2019) ALMA observations give an intrinsic source axial sizes of $100 \pm 18 \mu\text{as}$ (16.5–23.8 M) and $120 \pm 34 \mu\text{as}$ (17.3–31.0 M). Recent Sgr A* measurements of non-zero closure phase, e.g. $5.0^{+12.9}_{-4.6} \text{ }^\circ$ from measurements along the SMT-CARMA-APEX triangle (Lu et al. 2018), rule out a spherically symmetric emission profile.

3 PRINCIPAL GRMHD SIMULATIONS

We perform a set of three simulations using the conservative, 3D, ideal GRMHD code HARM (Gammie et al. 2003), which we denote as Standard And Normal Evolution (SANE), Magnetically Arrested Disc (MAD) and semi-MAD, all of which are endowed with electron temperature evolution based on Ressler et al. (2015). The simulations all have dimensionless spin $a = 0.5$, start from a

Fishbone & Moncrief (1976) torus, and have resolutions of $320 \times 256 \times 64$, uniform in the coordinates $x_1(r, \theta)$, $x_2(r, \theta)$, and $x_3 \equiv \varphi$, that are ‘cylindrified’ and hyper-exponentiated (Tchekhovskoy, Narayan & McKinney 2011) versions of modified Kerr–Schild (MKS) coordinates (McKinney & Gammie 2004, using $h = 0.3$), a process which is described in appendix B of Ressler et al. (2017). MKS coordinates focus resolution towards the mid-plane of the simulation, the ‘cylindrification’ process increases the angular width of cells with $r \lesssim 10M$, while the hyperexponentiation extends the radial extent of the grid to thousands of r_g by rapidly increasing the radial size of cells at $r > 400M$. The adiabatic index of the total gas is $\gamma = 5/3$ and the adiabatic index of the electrons is $\gamma_e = 4/3$, where the three simulations differ in both the size of the initial torus and the geometry of the initial magnetic field contained within this torus. The SANE initial torus has an inner boundary of $r_{\text{in}} = 12M$ and pressure maximum at $r_{\text{max}} = 24M$, while the semi-MAD and MAD initial tori have inner radii of $r_{\text{in}} = 15M$ and pressure maxima at $r_{\text{max}} = 34.5M$. While all simulations start with magnetic field lines that form single loops, the size and shape of the loops varies as determined by the magnetic vector potential, A_φ . A_φ scales as $A_\varphi \propto \rho$ in the SANE case and $A_\varphi \propto r^4 \rho^2$ in the semi-MAD case, both of which we normalize such that $\max(P)/\max(P_B) = 100$. The MAD vector potential is more complicated and is computed as described in Tchekhovskoy et al. (2011), while we normalize it such that $\min(P/P_B) = 100$. The resulting steady-state, time-averaged magnetic flux threading the horizon, Φ_{BH} , for each of the runs are $\ll 1M\sqrt{mc}$ (SANE), $\approx 40M\sqrt{mc}$ (semi-MAD), and $\approx 50M\sqrt{mc}$ (MAD).

The simulations implement the numerical density floor prescription $u_e \geq 0.01u_g$ from Ressler et al. (2015). The simulation grid concentrates 3D spatial resolution in the disc, allowing for non-axisymmetric turbulence, kink instabilities, etc., in the MHD flow. The code has been parallelized using message passing interface (MPI). The physical units of length and time are set by the mass of the black hole.

Our fiducial simulation is the semi-MAD run. We use a fiducial simulation time $T = 10\,000M$ to compare images and spectra. Time-averaged \dot{m} and \dot{E} are found to be nearly constant in radius for the inner $r < 35M$ for SANE, semi-MAD and MAD simulations alike, indicating that inflow and outflow equilibrium is obtained for the regions of interest in this work. In fact, the MAD simulation is in equilibrium up to $r \lesssim 100M$.

4 EMISSION MODELS

4.1 Electron Thermodynamic Models

4.1.1 Electron Evolution Model with Turbulent Heating

All of our simulations also include an electron entropy equation as described in Ressler et al. (2015) (neglecting electron conduction), using the Howes (2010) heating prescription for turbulent heating in collisionless plasmas. We refer to this as the ‘Electron Evolution Model with Turbulent Heating’ (or ‘Electron Evolution Model’ for short). Note that the Howes (2010) heating prescription is the result of calculations of the Landau damping of turbulence – different dissipation mechanisms at the end of a turbulent cascade could produce different results.

The Howes (2010) heating function is strongly dependent on plasma $\beta = P_g/P_B$, with a sharp transition between electrons being preferentially heated at $\beta \lesssim 1$ to protons being preferentially heated at $\beta > 1$. A direct consequence is that the relativistically

hot electrons are confined to the coronal and jet regions of the simulations, while the electrons in the mid-plane of the disc are non-relativistically cold.

4.1.2 Critical Beta Electron Temperature Model

In an attempt to mimic the behaviour of the Electron Evolution Model – without explicitly including turbulent heating in an entropy equation – we construct a post-processing function for the electron-to-total temperature ratio:

$$\frac{T_e}{T_{\text{tot}}} = f e^{-\frac{\beta}{\beta_c}}, \quad (1)$$

where $0 < f < 1$ is a constant, and β_c is the critical value of β that approximately sets a maximum β contributing to emission. We call this model the ‘Critical Beta Electron Temperature Model’ (or ‘Electron Temperature Model’ for short).

This model converges to unique values for the ratio T_e/T_p in the limits $\beta \rightarrow 0$ and $\beta \rightarrow \infty$ similarly to models in Mościbrodzka et al. (2014); Davelaar et al. (2018) employed by the EHT for M87 in which the ratio of proton-to-electron temperature is bounded by constants R_{low} and R_{high} .

4.1.3 Constant Electron Beta Model

Another viable post-processing prescription for the electron temperature is one in which the electron energy density u_e is some fixed fraction of the magnetic energy density u_B . This may be reasonable if magnetic reconnection is the dominant source of electron heating, as it is presumed to be in jet regions. This ‘Constant Electron Beta Model’ (or ‘Constant β_e Model’) is described by a single parameter through the relation $\beta_e = P_e/P_B = (\gamma_e - 1)u_e/(b^2/2) = \beta_{e0}$ (constant), or

$$P_e = \beta_{e0} P_B, \quad (2)$$

where $b^2 \equiv b^\mu b_\mu$.

Note that equipartition of particle and electromagnetic energies corresponds to $\beta_{e0} \sim 1$. Models coupling near-equipartition jets to Sgr A*’s accretion flow have previously been examined in Falcke, Mannheim & Biermann (1993) and Falcke & Markoff (2000). There, the jets have been invoked to explain the radio emission and, in some models, the higher frequency spectrum.

4.1.4 Magnetic Bias Model

We can generalize the Constant β_e Model so that the electron pressure scales as powers of the magnetic pressure

$$P_e = K_n P_B^n \sim b^{2n}, \quad (3)$$

where

$$K_n = K_1 \frac{\langle P_B \rangle}{\langle P_B^n \rangle} = 2^{n-1} K_1 \frac{\langle b^2 \rangle}{\langle b^{2n} \rangle} \quad (4)$$

and $\langle \rangle$ denotes an average over cylindrical radii $2M < R < 20M$ as in Table A1. We call this the ‘Magnetic Bias Model’ (or ‘Bias Model’ for short).

Note that $n = 1$, $K_1 \equiv \beta_{e0}$ corresponds to the Constant β_e Model. By default, for $n \neq 1$, we take $K_1 = 1$ in this work in the interest of space, although there is a priori no strong motivation for a particular value of K_n .

Table 1. Mass accretion rate yielding ≈ 2.4 Jy 230 GHz flux for our models. Negative values of mass accretion rate correspond to infall. The monochromatic flux is summed over $50M \times 50M$ image regions. For comparison, the Eddington accretion rate for Sgr A*’s mass is $-0.09 M_{\odot} \text{ yr}^{-1}$.

| Model | Accretion rate $M_{\odot} \text{ yr}^{-1}$ | | |
|---|--|-------------------------|-------------------------|
| | SANE | semi-MAD | MAD |
| Electron Evolution with Turbulent Heating | -2.61×10^{-8} | -1.70×10^{-8} | -1.44×10^{-11} |
| Critical Beta Electron Temperature (f, β_c) | | | |
| (0.1,0.01) | -1.11×10^{-7} | -1.72×10^{-7} | -1.90×10^{-9} |
| (0.1,0.1) | -8.10×10^{-8} | -1.16×10^{-7} | -4.31×10^{-10} |
| (0.1,1.0) | -6.92×10^{-8} | -9.14×10^{-8} | -2.58×10^{-10} |
| (0.5,0.01) | -2.57×10^{-8} | -3.62×10^{-8} | -3.11×10^{-10} |
| (0.5,0.1) | -1.52×10^{-8} | -1.13×10^{-8} | -7.87×10^{-11} |
| (0.5,1.0) | -3.93×10^{-9} | -6.06×10^{-9} | -2.15×10^{-11} |
| Constant Electron Beta (β_{e0}) | | | |
| 0.01 | -4.75×10^{-9} | -2.92×10^{-9} | -3.14×10^{-11} |
| 0.1 | -3.11×10^{-10} | -6.28×10^{-10} | -4.83×10^{-12} |
| 1.0 | -3.90×10^{-11} | -3.86×10^{-10} | -1.62×10^{-12} |
| Magnetic Bias (n) | | | |
| 0 | -4.04×10^{-9} | -1.41×10^{-9} | -1.66×10^{-9} |
| 1 | -3.90×10^{-11} | -3.86×10^{-10} | -1.62×10^{-12} |
| 2 | -2.21×10^{-11} | -4.54×10^{-10} | -1.95×10^{-12} |

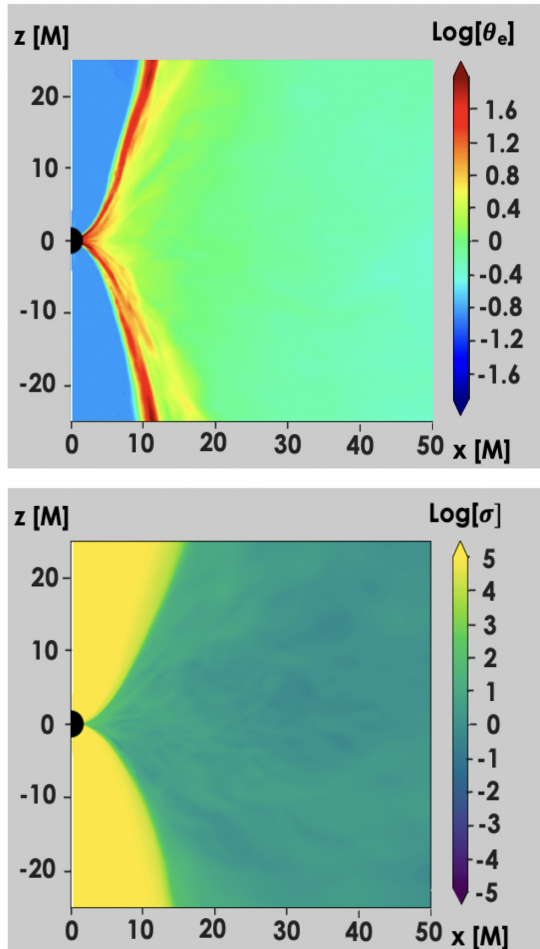


Figure 1. Slices of electron temperature $r\theta$ profile for the Electron Evolution Model (top) and slice of $\sigma = b^2/\rho$ (bottom). We use common log scales to present large dynamical ranges.

4.2 Radiative transport

We compute (mainly 230 GHz) images using the ray-tracing scheme IBOTHROS (Noble et al. 2007), which includes the effects of synchrotron emission and absorption, while we compute spectra using the Monte Carlo-based GRMONTY (Dolence et al. 2009), which includes the effects of synchrotron emission, absorption, and inverse-Compton scattering. For the purposes of radiative transport, we exclude regions of the simulation with $\sigma \equiv b^2/\rho > 1$ where the GRMHD solution becomes less reliable. The pixel resolution used to produce IBOTHROS images in this work is $1M$ per pixel in both directions.

Since GRMHD simulations are scale free, for each electron temperature model we choose the physical mass unit such that the flux at 230 GHz matches the 2.4 Jy measurement (Doeleman et al. 2008) (to < 2 per cent). Table 1 lists the resulting mass accretion rate for each of our models. Note that negative accretion rate corresponds to inflow.

Our fiducial viewing angle will be 90 deg (edge-on disc) and our fiducial observer frequency will be $\nu_{\text{Obs}} = 230$ GHz, though we also consider 0 deg (face-on disc), 45 deg, and $\nu_{\text{Obs}} = 140$ THz, the latter for comparison with near-infrared observations. In the absence of other labels, all of the images and spectra shown correspond to fiducial values of viewing angle and frequency and to the semi-MAD simulation.

5 RESULTS

5.1 Electron temperature profiles

Fig. 1 shows the azimuthally averaged electron temperature distribution for the Electron Evolution Model and plasma electromagnetic-to-particle flux density σ in the $r\theta$ plane. The electron temperature is greatest on the boundary between the high σ outflow and lower σ outflow and inflow as found in Ressler et al. (2015). Fig. 2 shows the azimuthally averaged electron temperature distributions in the $r\theta$ plane resulting in each of our models for a few select parameter choices. For Critical Beta Electron Temperature Models,

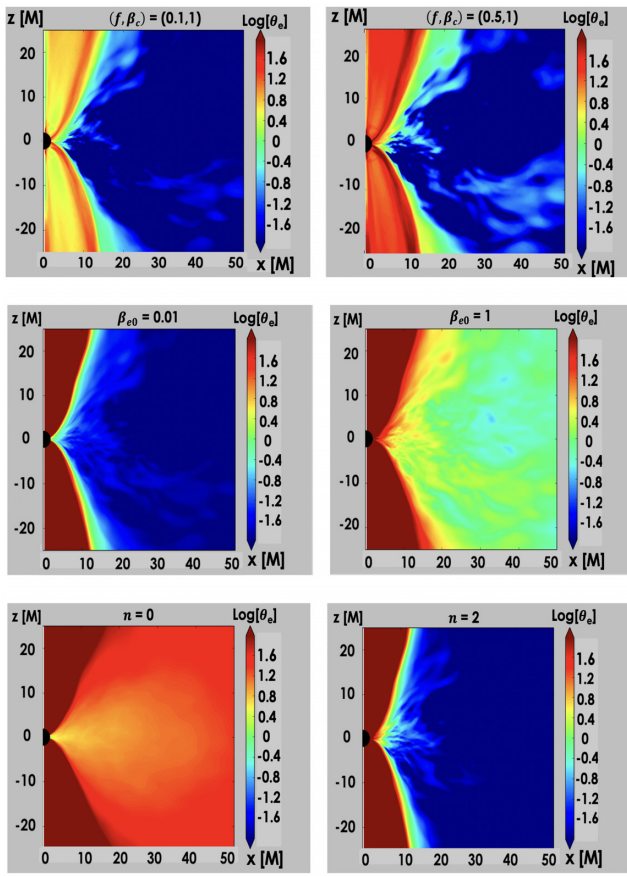


Figure 2. Electron temperature $r\theta$ profiles for the Critical Beta Electron Temperature Model with $(f, \beta_c) = (0.1, 1)$ (top left) and $(0.5, 1)$ (top right). Also, electron temperature $r\theta$ profiles for Constant β_e Models with $\beta_{e0} = 0.01$ (middle left), $\beta_{e0} = 1$ (middle right), and Bias Models with $n = 0$ (bottom left), and $n = 2$ (bottom right). The temperature is expressed in dimensionless form $\theta_e = k_B T_e / m_e c^2$.

a boundary layer on the disc-jet interface (mild outflow+corona) is the region with highest T_e . This behaviour is consistent throughout the parameter space $f \in \{0.1, 0.5\}$ and $\beta_c \in \{0.01, 0.1, 1\}$.

The electron temperature profiles in various Constant β_e Models in the middle panels of Fig. 2 are hottest for the strong interior outflow, or ‘spine,’ characterized by low density and high magnetization. In Bias Models at the bottom panels of Fig. 2, electron temperature is also highest near the coherent, electromagnetically dominated outflow. Now, however, the radial profile is strongly dependent on the exponent n , which enhances the variation of emission (a function of b) with cylindrical radius in the simulation.

5.2 Electron Evolution Model with Turbulent Heating

5.2.1 Electron Evolution Model images

The Electron Evolution Model image³ in Fig. 3 shows a ring of lensed emission around the black hole event horizon and a

³Each individual pixel in the image plane (normal to the observer) has an $I_\nu = dF_\nu/d\Omega$ in cgs units, and $F_{\text{tot}} \approx 2.4 \times 10^{-23} \text{ erg s}^{-1} \text{ cm}^{-2} \text{ Hz}^{-1} = 2.4 \text{ Jy}$ is just the sum of all the dF_ν ’s. Thus, multiply each cgs intensity coloured pixel value by 57.9 to get its flux density in Jy.

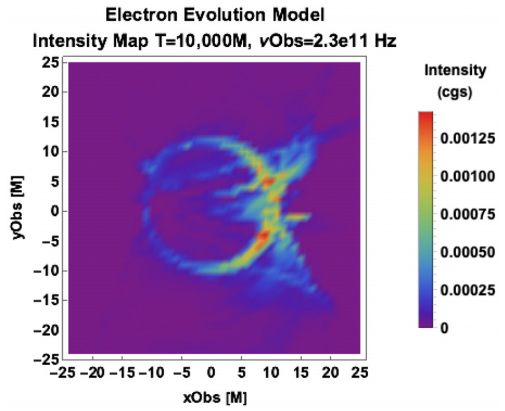


Figure 3. Electron Evolution Model image at 230 GHz.

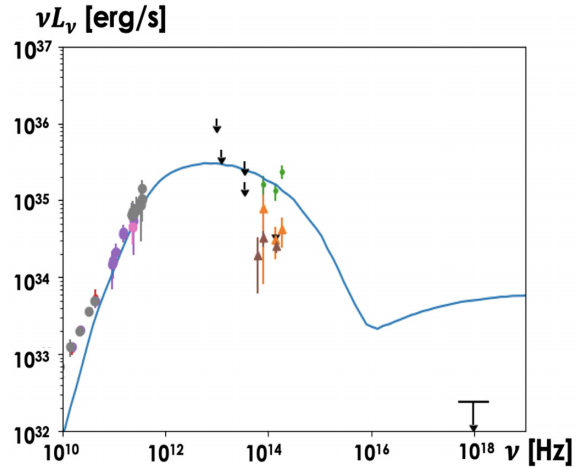


Figure 4. Spectrum generated from the Electron Evolution Model with turbulent heating.

small outflow: the wispy outflow is visible at radii not exceeding $30M$ and is limb brightened. Asymmetry in the photon ring is apparent due to Doppler shifts at the edge on viewing angle. The images in this paper are rendered in observer coordinates left-right and up-down inverted relative to Ressler et al. (2017). In our implementation of a new imaging pipeline 90 deg inclination has the accretion flow approaching on the right and black hole spin pointing down.

5.2.2 Electron Evolution Model spectra

The Electron Evolution Model spectrum is shown in Fig. 4. The infrared bump is well fit; however, the model’s low-frequency slope steepens under the data around 10 GHz, and the model significantly overpredicts the X-ray emission. Note that this spectrum also appears in Ressler et al. (2017).

5.3 Critical Beta Electron Temperature Model

5.3.1 Electron Temperature Model images

The images in Fig. 5 show the β_c variation of the Electron Temperature Model for $f = 0.1$ and $f = 0.5$, respectively. For most of

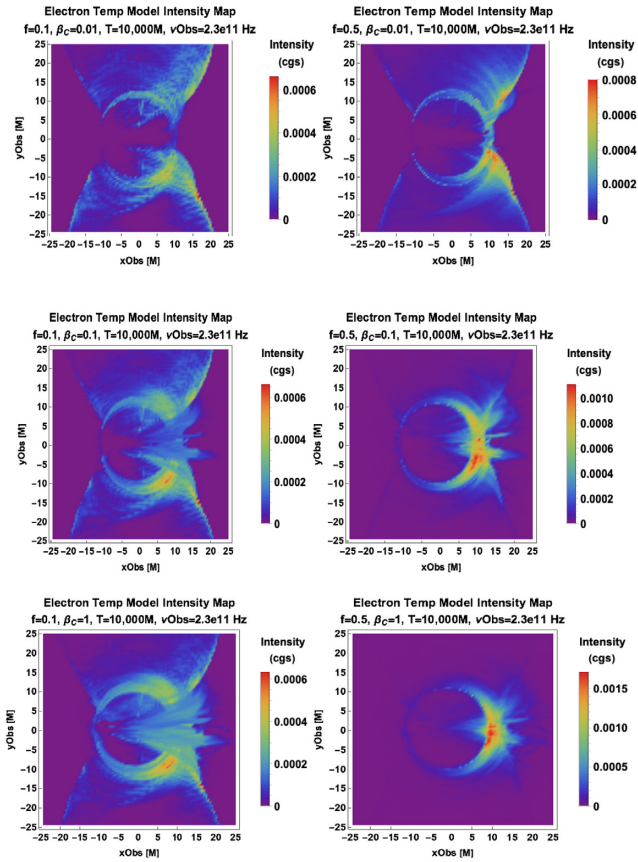


Figure 5. Critical Beta Electron Temperature Model images for $f = 0.1$ (left-hand panels) and $f = 0.5$ (right-hand panels) for $\beta_c = 0.01$ (top panels), $\beta_c = 0.1$ (middle panels), and $\beta_c = 1$ (bottom panels).

the parameter space, the Electron Temperature Model appears to be a fairly uniform projection of the inflow–outflow boundary/coronal region. For the highest values of f and β_c , the images become more asymmetric and the outflow is limited to smaller radii. Optical depth effects are apparent as follows. In the optically thin case, the prescription $T_e = f T_{\text{pe}} e^{-\beta/\beta_c}$ at constant β_c has line-of-sight intensity proportional to f ; yet the brightness of intensity maps in Fig. 5 are not simple re-scalings of each other as a function of f . This is most noticeable at the highest value $\beta_c = 1$, where the intensity map appears several times more compact and lopsided as we vary f from 0.1 to 0.5.

5.3.2 Electron Temperature Model spectra

Electron Temperature Model spectra generated with parameter values $(f, \beta_c) = (0.1, 1)$ and $(0.5, 1)$ are shown in Fig. 6. Increasing the overall electron temperature pre-factor f at constant β_c is seen to increase the width of the synchrotron peak – reflecting a greater range of emitting temperatures. For $(f, \beta_c) = (0.5, 1)$, the model fits data points over a broad frequency range: from microwaves to infrared to X-rays, with possible improvement in the NIR with the addition of non-thermal electrons (and slight reduction in f, β_c if this introduces an X-ray excess). From our parsimonious set of two assumptions regarding high and low β electron temperature behaviour, the simple parametrized Electron Temperature Model performs comparably to the full electron evolution calculation. In fact, for $(f, \beta_c) = (0.5, 1)$, the Critical Beta Electron Tempera-

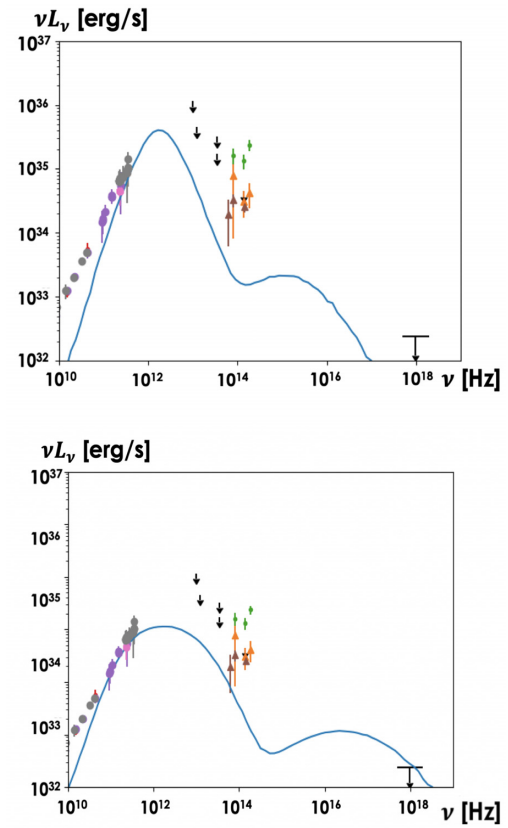


Figure 6. Spectra generated from $(f, \beta_c) = (0.1, 1)$ (top Panel) and $(0.5, 1)$ (bottom panel) Critical Beta Electron Temperature Models.

ture Model is in better agreement with observations at the high-frequency end.

5.4 Constant Electron Beta Model

5.4.1 Constant β_e Model images

Constant β_e Model images are presented for $\beta_{e0} = 0.01, 0.1$, and 1 in the top and middle panels of Fig. 7. The images are comprised of a thick torus of lensed disc emission starting at the innermost photon rings and surrounded by dimmer filaments. Decreasing the parameter β_{e0} decreases the electron temperature and leads to thinner tori of disc emission and increasing outflow-to-inflow ratio of filamentary emission. In this limit as well, we find increasing asymmetry as the photon rings emission wane into a narrow crescent on one side. The increased asymmetry is quantified in Table A2; the centroid of the image for $\beta_{e0} = 0.01$ has the furthest lateral displacement for all our models.

5.4.2 Constant β_e Model spectra

Constant β_e Model spectra for $\beta_{e0} = 0.01$ and 0.1 are shown in Fig. 8 excluding regions $r > 30M$ that are not in equilibrium. These spectra generally reproduce the low-frequency slope well, though flatten near the infrared bump – particularly for lower values of the constant β_e . The radio spectra can be explained in the context of the Blandford–Königl model (Blandford & Königl 1979), which demonstrates that helical magnetic fields and constant β_e in outflows that are optically thick to synchrotron emission

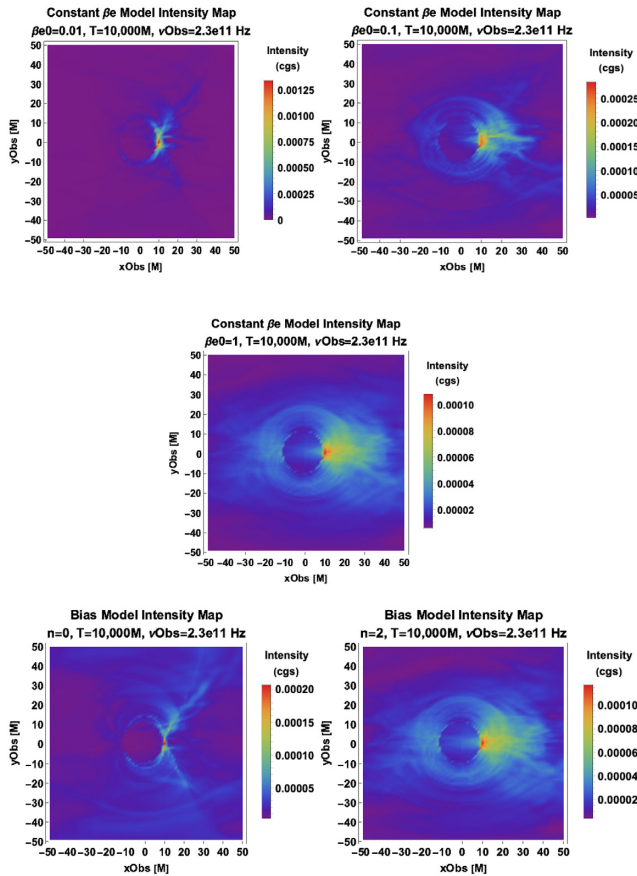


Figure 7. Constant β_e Model image for $\beta_{e0} = 0.01$ (top left) $\beta_{e0} = 0.1$ (top right) and $\beta_{e0} = 1$ (centre), along with Bias model images for $n = 0$ (bottom left) and $n = 2$ (bottom right).

produce radio spectra that are flat in L_ν , consistent with the low-frequency emission in Sgr A*. The spectral slope rises in the X-ray, as outflow/jet emission overproduces the high-frequency spectrum.

5.5 Magnetic Bias Model

5.5.1 Bias Model images

From equation (3), it is manifest that the simplest ($n = 0$) Bias Model has constant relativistic electron gas pressure throughout the simulation, in contrast to its expected decrease along the outflow for higher values of n . The image in the bottom left-hand panel of Fig. 7 for $n = 0$ shows extended emission tracing a funnel shape in the jet/outflow region. For $n = 2$, emission becomes dominated by a thick photon torus lensed orthogonally to the accretion disc.

For Bias Model images, decreasing n leads to more extended outflow contributions to emission. The Bias and Constant β_e models have the most drastic variation of image intensity and shape over the observer plane for the models considered in this work.

5.5.2 Bias Model spectra

Spectra for Bias Models with $n = 0$ and 2 are shown in Fig. 8. The $n = 2$ model dramatically overproduces the emission at IR–X-rays. Both the $n = 0$ and $n = 2$ models do a reasonable job of explaining the low frequency radio emission, which is not surprising since

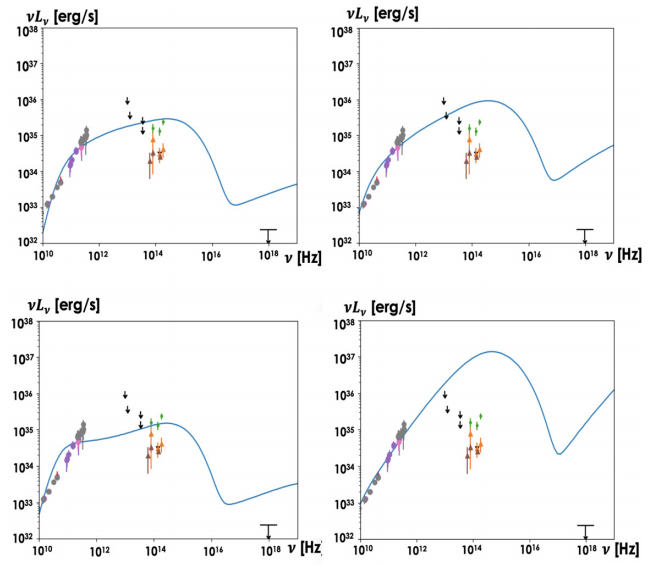


Figure 8. Observed spectra (dots) compared with Synthetic Model spectra (curves) generated from $\beta_{e0} = 0.01$ model (top left), $\beta_{e0} = 0.1$ model (top right), $n = 0$ bias model (bottom left), and $n = 2$ bias model (bottom right).

these models are generalizations of the constant β_e model known to explain the radio emission in optically thick AGN jets.

5.6 EHT and GRAVITY

Dexter et al. (2010) fit Sgr A* thermal synchrotron emission models parametrized by mass accretion rate, orientation angle, spin and electron-to-proton temperature ratio to mm-VLBI, and spectral data (Marrone 2006), favouring a wide 50 deg viewing angle. Our view of the Galactic Centre has evolved, as GRAVITY has provided indications from infrared observations that the Galactic Centre inner disc (between $6M$ and $10M$) appears more face on (Gillessen et al. 2017).

We now compare synthetic EHT-scale (230 GHz) images against GRAVITY-scale (2.2 μ m, or 1.4 THz) images for a particular model, $(f, \beta_c) = (0.5, 1)$, in Fig. 9, varying the viewing angle from face-on to edge-on (note, we display these on a common log scale to accentuate features). The face-on disc has smoother variation of intensity with radius at 230 GHz, as it slowly goes from spiral edges to circular at $r \sim 10M$ to the innermost stable circular orbit. At 2.2 μ m, the disc appears spiral throughout, punctuated with distinct bright spots. At 45 deg inclination, the brightest feature at both frequencies is a circular ring with $r \lesssim 15M$. The edge-on view exhibits greater disc asymmetry due to Doppler brightening at 230 GHz, and has a more prominent outflow with more apparent substructure at 2.2 μ m.

We see the dynamical behaviour of the $(f, \beta_c) = (0.5, 1)$ model at IR frequency in Fig. 10, where we show face-on images at several different times. The bright spots appear to rotate on time-scales between $\Delta T = 100M$ and $1000M$, where $M = 20s$. The image symmetry makes the centroid motion localized to small gyrations centred on the black hole for this model.

5.7 SANE versus semi-MAD versus MAD Simulations

SANE, magnetically arrested disc (MAD) and semi-MAD simulations, represents quite distinct forms of evolution of magnetized

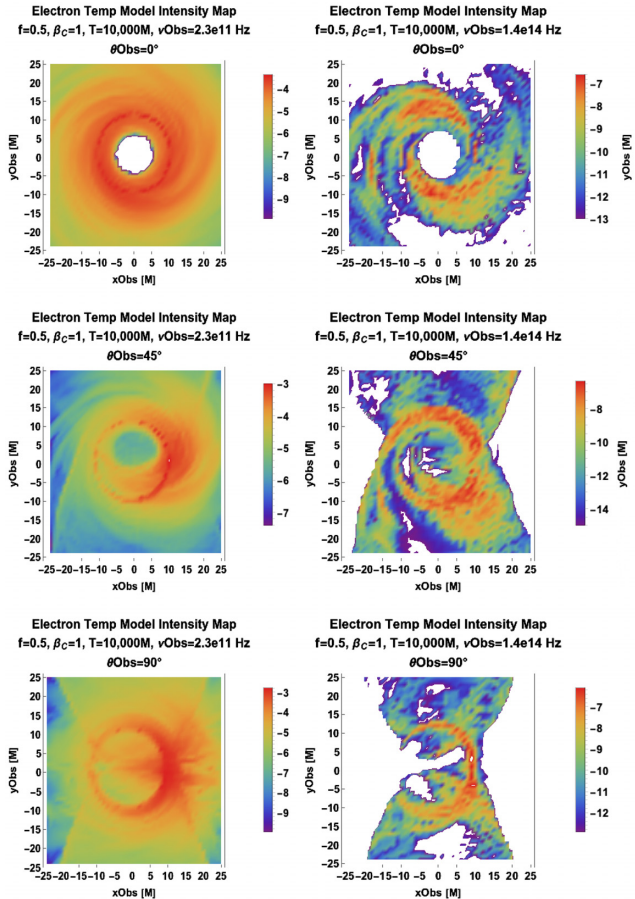


Figure 9. EHT scale (230 GHz, left) versus GRAVITY scale (140 THz, right) log plot images of the favoured $(f, \beta_c) = (0.5, 1)$ model. The observer angle varies from $\theta_{\text{Obs}} \approx 0$ to $\frac{\pi}{4}$ to $\frac{\pi}{2}$ from top to bottom. These image maps are shown on a log scale in order to accentuate features in the intensity profiles.

accretion flows. The SANE case has the lowest magnetic flux; the MAD case admits the lowest amount of mass accreted by the black hole, as in Table 1. Compared to images ray traced from the fiducial semi-MAD simulation, the SANE and MAD images vary in size and asymmetry in a similar manner with changing parameters in our models. For example, Fig. 11 shows that increasing Critical Beta Electron Temperature Model parameter f from 0.1 to 0.5 takes a relatively symmetric photon ring/torus and extended outflow structure to a compact, asymmetric ring for all three simulations. The same trend holds for increasing β_c from 0.01 to 1. For the $f=0.5$ models in all three simulations, a disc feature is visible emanating from the bright-spot and extending along the projected equatorial plane. It is also noteworthy that the best $10^{11} \text{ Hz} < v_{\text{Obs}} < 10^{19} \text{ Hz}$ spectrum across simulations (cf. Fig. 12) corresponds to the $(f, \beta_c) = (0.5, 1)$ model in the semi-MAD simulation; however, the MAD simulation for this model generates the best low frequency fit. We do add the caveat that with the addition of non-thermal particles, we expect the MAD images to have increased NIR and X-ray contributions. As for other models, decreasing Constant Electron Beta Model Parameter β_{e0} from 1 to 0.01 changes images from thick photon tori to thin rings+outflows. Decreasing Magnetic Bias Model parameter n from 2 to 0 accentuates the outflow in all three simulations, with the key difference being greatest collimation in the SANE simulation. For all simulations and models, inclusion

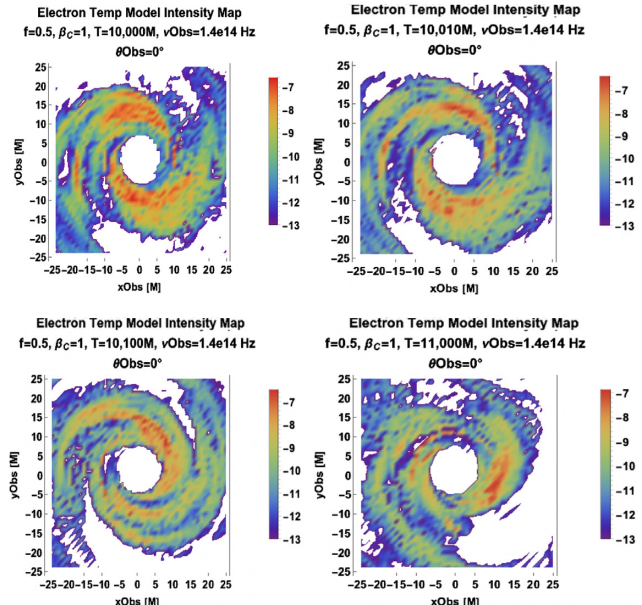


Figure 10. A sequence of face-on $(f, \beta_c) = (0.5, 1)$ model infrared images at $T = 10\,000M, 10\,010M, 10\,100M$ and $11\,000M$. Variation can be observed after a hundred M , but the basic spiral morphology with bright spots is maintained over at least a thousand M .

of non-thermal particles could readily increase the IR and X-ray emissions.

5.8 mm/NIR variability

In Fig. 13, we display mm and NIR light curves for select models. The models exhibit different variability time-scales, e.g. doubling times, over the $4000M$ (≈ 24 h) interval depicted. The $\beta_{e0} = 1$ and $n = 2$ models exhibit the mildest variation of a few per cent within an hour ($\approx 160M$). These models are immediately precluded if we require at least minute-scale variability. The $n = 0$ model is slightly more variable, with slightly larger amplitude local minima and maxima. The $(f, \beta_c) = (0.5, 1)$ model is the most rapidly varying, followed by $(f, \beta_c) = (0.1, 1)$. The greatest amplitude flare-like feature in the radio is the twofold peak-to-trough variation for $12\,700M \lesssim t_{\text{obs}} \lesssim 13\,500M$ in the $\beta_{e0} = 0.01$ model light curve.

The NIR luminosity differs by orders of magnitude among the models in Fig. 13. The models with the greatest overall flux are for $n = 2$ and $\beta_{e0} = 1$. The lowest flux model, $(f, \beta_c) = (0.5, 1)$, exhibits the fastest peak-to-trough variability and the largest percentage swings. But despite these large relative excursions from the mean flux, the low absolute amplitude NIR luminosity suggests that this model requires a non-thermal particle contribution.

5.8.1 Time averaging

We have primarily compared models at a particular time $T = 10\,000M$ for which the simulation flow is statistically in steady state. However, given the 20s light crossing time of Sgr A*'s gravitational radius, variability challenges EHT's temporal imaging capacity for Sgr A* – and all but the most massive black holes. Fig. 14 shows an image averaged over $1000M$ (6 h for Sgr A*) for our $(f, \beta_c) = (0.5,$

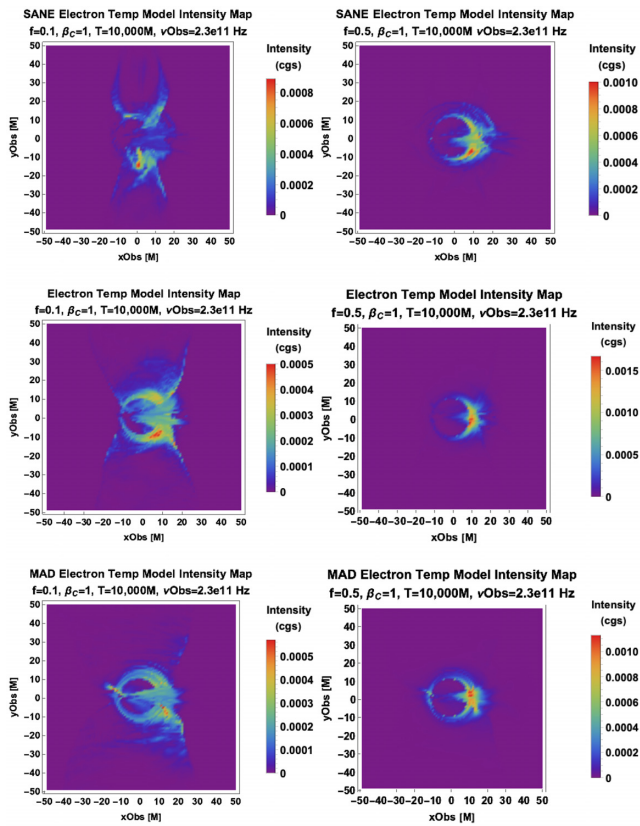


Figure 11. Critical Beta Electron Temperature Model for $f = 0.1$ (left-hand panels) and $f = 0.5$ images (right-hand panels) for $\beta_c = 1$ SANE (top panels), semi-MAD (middle panels), and MAD simulations (bottom panels).

1) model. The result is very similar to the instantaneous image in Fig. 5. Examining time evolution of the image in detail, we find that there is image variability on roughly hourly time-scales, with some bright features moving around. The overall image morphology is, however, relatively stable.

6 COMPARISON OF MODELS

We now synthesize our results to assess that models are favoured by observations, starting with our fiducial semi-MAD simulation. A summary of how the different models fare against observational constraints is given in Table A3.

6.1 Comparison of images

In the images for the Electron Evolution Model with turbulent heating, the emission is concentrated in an asymmetric photon ring, with some contribution from outflow at small radii. The Critical Beta Electron Temperature Model images have emission smeared out broadly over inflow and outflow at low f or β_c , and approach a compact, asymmetric photon ring for $(f, \beta_c) \rightarrow (0.5, 1)$, with even less outflow contribution relative to the Electron Evolution Model. The Constant β_e and Bias models have drastically varying morphology over the parameter space scanned – from long, extended outflow filaments for the low β_{e0} and low n models, to thick photon tori in the high β_{e0} and high n limits.

The relative asymmetry of model images can be compared using image moments in Table A2, where models in which most of the

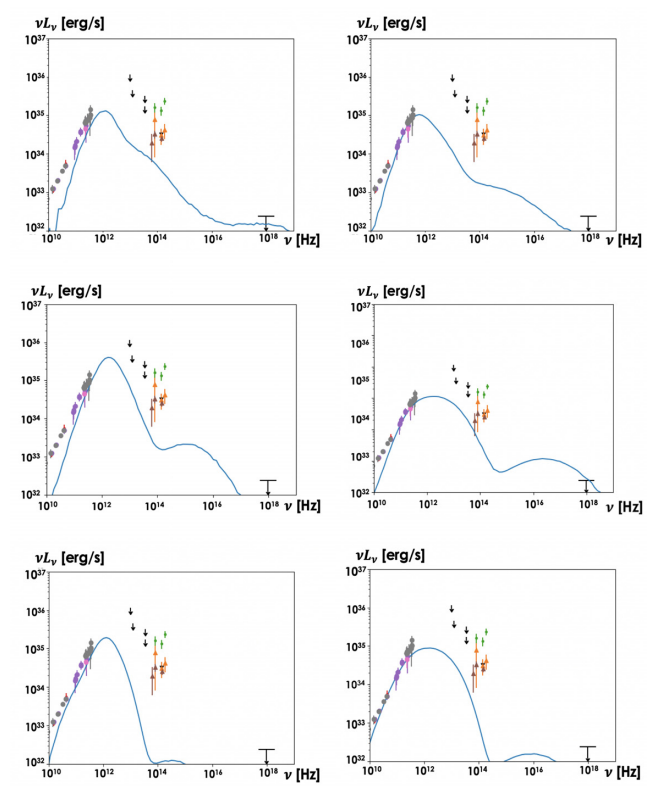


Figure 12. Critical Beta Electron Temperature Model $f = 0.1$ (left-hand panels) and $f = 0.5$ spectra (right-hand panels) for $\beta_c = 1$ SANE (top panels), semi-MAD (middle panels), and MAD simulations (bottom panels).

flux density emanates from compact regions such as $\beta_{e0} = 0.01$ or $(f, \beta_c) = (0.5, 1)$ are shown to have centroids shifted furthest to the right in our fiducial simulation. We make further quantitative comparisons of the images by ascribing emitting region sizes to our intensity maps.

6.1.1 Emitting region

We adopt the image covariance approach that Johnson et al. (2018) used to derive the $9.87M < \theta_{\text{maj,Obs}} < 12.69M$ elliptical Gaussian size constraint for 230 GHz Sgr A* EHT observations to formulate characteristic emitting region sizes for our synthetic images. The intensity can be expressed as a moment generating function

$$\tilde{I}(\mathbf{u}) = \int d^2\mathbf{x} I(\mathbf{x}) e^{-2\pi i \mathbf{u} \cdot \mathbf{x}}. \quad (5)$$

The image covariance matrix is

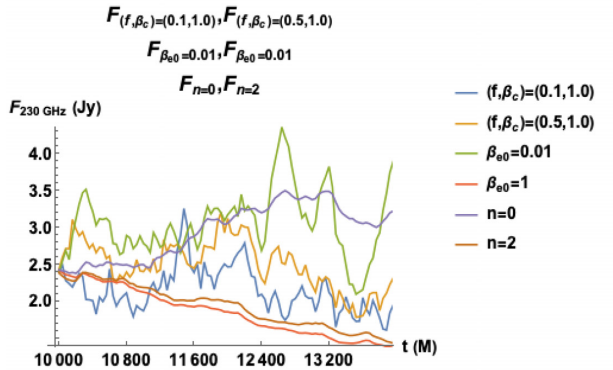
$$M = \begin{pmatrix} \frac{M_{20}}{M_{00}} - \left(\frac{M_{10}}{M_{00}}\right)^2 & \frac{M_{11}}{M_{00}} - \frac{M_{10}M_{01}}{M_{00}^2} \\ \frac{M_{11}}{M_{00}} - \frac{M_{10}M_{01}}{M_{00}^2} & \frac{M_{02}}{M_{00}} - \left(\frac{M_{01}}{M_{00}}\right)^2 \end{pmatrix}, \quad (6)$$

where

$$M_{n1,n2} = \sum_{i,j} x_i^{n1} y_j^{n2} I(x_i, y_j). \quad (7)$$

The equivalent Gaussian FWHM for images in Observer Plane coordinates is

Model mm Light Curves:



Model NIR Light Curves:

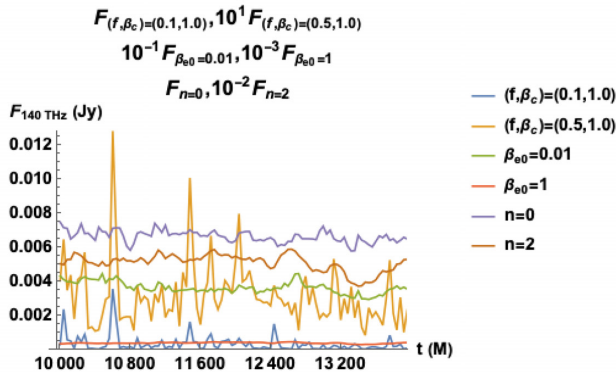


Figure 13. Light curves at 230 GHz (top) and 140 THz (bottom) for parametric models with $(f, \beta_c) = (0.1, 1)$, $(f, \beta_c) = (0.5, 1)$, $\beta_{e0} = 0.01$, $\beta_{e0} = 1$, $n = 0$, and $n = 2$.

$$(\theta_{\text{maj}})_{\text{Obs}} = \sqrt{-\frac{2 \ln 2}{\pi^2 \int d^2 x I(x)}} \times \sqrt{\left((\hat{u}_{\text{maj}})_1^2 \frac{\partial^2 \tilde{I}}{\partial u_1^2} + 2(\hat{u}_{\text{maj}})_1 (\hat{u}_{\text{maj}})_2 \frac{\partial^2 \tilde{I}}{\partial u_1 \partial u_2} + (\hat{u}_{\text{maj}})_2^2 \frac{\partial^2 \tilde{I}}{\partial u_2^2} \right)} = 2 \sqrt{2 \ln 2 \frac{(\hat{u}_{\text{maj}})_1^2 M_{20} + 2(\hat{u}_{\text{maj}})_1 (\hat{u}_{\text{maj}})_2 M_{11} + (\hat{u}_{\text{maj}})_2^2 M_{02}}{M_{00}}} \quad (8)$$

where \hat{u}_{maj} is the eigenvector of the covariance matrix corresponding to greatest eigenvalue λ_{maj} and \hat{u}_{min} is defined analogously. We may conceptualize $(\theta_{\text{maj}})_{\text{Obs}}$ as a normalized second directional derivative along the image major axis. We take our characteristic image size to be the centroid-adjusted equivalent Gaussian FWHM:

$$\theta_{\text{maj}} = 2 \sqrt{(2 \ln 2) \lambda_{\text{maj}}}. \quad (9)$$

In Table 2, using the elliptical Gaussian size constraint, we have the following trends in image size.

- (i) Image size decreases with f or β_c .
- (ii) Image size increases with β_{e0} (with the exception of the SANE simulation at low β_{e0}).
- (iii) Image size decreases with n (exceptions: high n SANE and MAD).

The preferred models with smallest size occur for $(0.5, 1)$, particularly in the SANE simulation, which satisfies the EHT size constraint for θ_{maj} .

Electron Temp Model Intensity Map

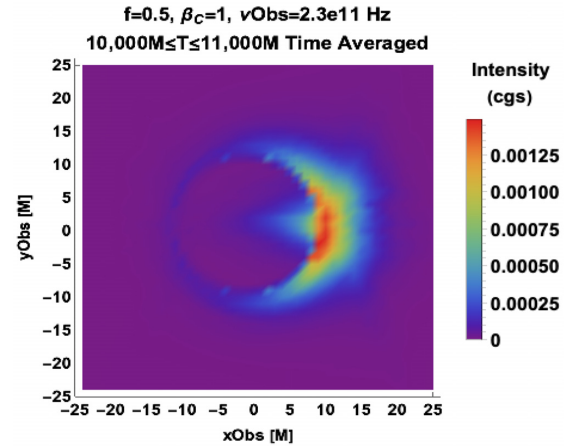


Figure 14. Preferred model $[(f, \beta_c) = (0.5, 1)]$ averaged over simulation times $10,000M < T < 11,000M$ at 230 GHz.

Note that observational effects such as scattering, the point spread function and instrument-specific cadence tend to wash out image features. While we do not include a model for scattering in this work, we have time-averaged our preferred model in Fig. 14 to reflect uncertainties due to temporal resolution. The time averaged image for the ~ 6 h interval $10,000M < T < 11,000M$ is similar to the instant one in Fig. 5 (lower right), and the spectral shape does not vary appreciably even over the ~ 12 h interval $9,000M < T < 11,000M$, as discussed in Section 5.8.1.

6.1.2 Image size frequency and viewing angle dependence

In Table 3, image sizes are compared at angles 0 deg (face on) versus 90 deg (edge on) and frequencies 86 GHz [Global mm VLBI Array (GMVA)] versus 230 GHz (EHT). For both frequencies, the edge-on image sizes tend to decrease with each of f and β_c , increase in β_{e0} and decrease in n ; the face-on images do not exhibit monotonic behaviour. Moreover, at a given frequency, the edge-on images tend to be larger than their face-on parametric counterparts for Critical β Models [except at high (f, β_c)]; face-on images are larger than edge-on images for the Constant β_e Model (except at low β_{e0}) and Magnetic Bias Model (except at higher frequency and low n). Face on and at low frequency, intensity profiles appear broad and point symmetric due to the projection of co-axial outflows and disc on to the observer plane – particularly for low n and low (f, β_c) . The smallest of our flux-normalized images tend to occur for the most asymmetric models, e.g. $(f, \beta_c) = (0.5, 1)$.

The images satisfying the 86 GHz size constraint occur for the Critical Beta Electron Temperature models $(f, \beta_c) = (0.1, 0.01)$, $(0.1, 0.1)$, $(0.1, 1)$, $(0.5, 0.01)$, $(0.5, 0.1)$, and $(0.5, 1)$ for the SANE and MAD simulations and MAD $\beta_e = 0.01, 0.1$, and 1 Constant β_{e0} and $n = 0, 1$, and 2 Bias models viewed at 0 deg; and the $(f, \beta_c) = (0.5, 1)$ model for the SANE, semi-MAD, and MAD simulations at 90 deg. The unique model satisfying the 230-GHz size constraint is the $(f, \beta_c) = (0.5, 1)$ model in the SANE simulation viewed edge on.

6.2 Comparison of spectra

The Electron Evolution Model with Turbulent Heating fits most of the data near the sub-mm bump. Spectra in models inspired

Table 2. Elliptical Gaussian semiaxes θ_{\min} and θ_{\max} generated from second-order central image moments and image covariance matrices for our models for SANE, MAD, and semi-MAD simulations at the fiducial 230 GHz frequency and 90 deg (edge-on) viewing angle. The anisotropic observational size constraints are $5.44M < \theta_{\min} < 10.68M$ and $9.87M < \theta_{\max} < 12.69M$ (Johnson et al. 2018).

| Model | $\frac{\theta_{\min}}{M} = \sqrt{(8 \ln 2) \lambda_{\min}}$ | | | $\frac{\theta_{\max}}{M} = \sqrt{(8 \ln 2) \lambda_{\max}}$ | | |
|---|---|------------|------|---|----------|------|
| | SANE | Semi-MAD | MAD | SANE | Semi-MAD | MAD |
| Electron Evolution with Turbulent Heating | 8.2 | 9.0 | 11.4 | 18.2 | 15.3 | 15.1 |
| Critical Beta Electron Temperature (f, β_c) | | | | | | |
| (0.1, 0.01) | 9.4 | 24.7 | 38.9 | 28.8 | 48.4 | 73.1 |
| (0.1, 0.1) | 8.8 | 21.8 | 18.5 | 24.7 | 39.7 | 34.2 |
| (0.1, 1.0) | 8.8 | 20.8 | 15.0 | 22.3 | 33.6 | 23.7 |
| (0.5, 0.01) | 9.4 | 33.6 | 25.0 | 29.2 | 43.7 | 55.9 |
| (0.5, 0.1) | 8.7 | 16.8 | 19.1 | 22.8 | 24.4 | 34.2 |
| (0.5, 1.0) | 9.3 | 15.3 | 12.5 | 11.7 | 18.5 | 14.3 |
| Constant Electron Beta (β_{e0}) | | | | | | |
| 0.01 | 14.9 | 22.7 | 22.5 | 45.7 | 44.2 | 44.2 |
| 0.1 | 19.0 | 45.4 | 47.2 | 26.9 | 46.7 | 53.4 |
| 1.0 | 37.2 | 45.9 | 57.7 | 39.7 | 56.0 | 58.7 |
| Magnetic Bias (n) | | | | | | |
| 0 | 43.7 | 58.6 | 30.2 | 75.1 | 66.9 | 75.3 |
| 1 | 37.2 | 45.9 | 57.7 | 39.7 | 56.0 | 34.2 |
| 2 | 30.7 | 43.1 | 60.5 | 47.3 | 52.9 | 62.8 |

Table 3. Elliptical Gaussian semi-axes θ_{\min} and θ_{\max} generated from second-order central image moments and image covariance matrices for our semi-MAD models at varying viewing angles (0 deg versus 90 deg) and frequencies (86 versus 230 GHz). The anisotropic size constraints are $5.44M < \theta_{\min} < 10.68M$ and $9.87M < \theta_{\max} < 12.69M$ at 230 GHz and $16.5 < \theta_{\min} < 23.8M$ and $17.3M < \theta_{\max} < 31.0M$ at 86 GHz (Issaoun et al. 2019).

| Model | $\theta_{\min}(M)$ | | $\theta_{\max}(M)$ | | | |
|---|--------------------|-------------------|--------------------|------------------|-------------------|-------------------|
| | 86 GHz, 0 deg | 86 GHz, 90 deg | 230 GHz, 0 deg | 86 GHz, 0 deg | 86 GHz, 90 deg | 230 GHz, 0 deg |
| Electron Evolution | 37.6 | 25.7 | 26.8 | 39.7 | 47.8 | 28.5 |
| Electron Temperature (f, β_c) | | | | | | |
| (0.1, 0.01) | 43.7 | 30.4 | 33.8 | 54.7 | 69.7 | 39.1 |
| (0.1, 0.1) | 39.8 | 29.6 | 28.9 | 48.7 | 62.5 | 32.2 |
| (0.1, 1.0) | 50.6 | 29.6 | 25.9 | 45.5 | 56.4 | 28.6 |
| (0.5, 0.01) | 42.5 | 28.4 | 34.9 | 47.6 | 59.5 | 39.5 |
| (0.5, 0.1) | 36.6 | 28.7 | 25.7 | 38.4 | 38.6 | 27.2 |
| (0.5, 1.0) | 33.9 | 27.6 | 24.3 | 34.8 | 29.4 | 25.4 |
| Constant Electron Beta (β_{e0}) | | | | | | |
| 0.01 | 44.1 | 32.9 | 40.1 | 48.2 | 49.9 | 42.1 |
| 0.1 | 56.6 | 45.8 | 54.0 | 59.5 | 50.3 | 57.6 |
| 1.0 | 61.5 | 45.7 | 61.5 | 62.8 | 57.0 | 62.9 |
| Magnetic Bias (n) | | | | | | |
| 0 | 64.5 | 58.8 | 63.5 | 66.9 | 62.0 | 66.2 |
| 1 | 61.5 | 45.7 | 61.5 | 62.8 | 57.0 | 62.9 |
| 2 | 60.7 | 44.4 | 58.9 | 62.6 | 55.0 | 61.1 |

by equipartition (Constant β_e and Bias) are dominated by near-horizon outflow emission (this becomes more apparent in images at lower frequencies, as the lensed disc becomes less prominent). These spectra significantly overproduce frequencies above infrared. For the Bias Model, lower n reduces the fall-off of u_e with radius, accounting for flatter radio and X-ray spectra. Spectra in the Critical Beta Electron Temperature Model tend to be dominated by outflow or coronal emission, especially at lower f or β_c , and tend to be more peaked than the data.

The following summarizes trends appearing upon comparing spectra in different models:

- (i) The Critical Beta Electron Temperature Model reproduces low- and high-energy spectral amplitudes over the 10^{11} – 10^{19} Hz frequency domain better than the Constant β_e and Bias models.
- (ii) The radio–IR spectrum is flatter for lower β_{e0} in the Constant β_e Model.

(iii) The radio–IR spectrum is flatter for lower n in the Bias Model (until a sharp low-frequency turnover at $\lesssim 10^{11}$ Hz, where lower n models steepen).

(iv) Spectra in the Constant β_e and Bias Models appear flatter than spectra in the Critical Beta Electron Temperature Model.

Some of these trends are a consequence of varying mass accretion rate and synchrotron absorption in different models, as discussed below.

6.2.1 Trends with mass accretion rate

From Table 1, model families with flatter spectra (Constant β_e and Bias Models) tend to have lower (magnitude) mass accretion rates than the family with steeper spectra (the Critical Beta Electron Temperature Model). This can be explained from the simulation as follows. As $|\dot{m}|$ decreases at fixed flux at 230 GHz, temperature increases and plasma in regions that have not previously been emitting synchrotron radiation begin to emit, broadening the range of emitting temperatures and, in turn, the spectra. This also predicts an anticorrelation between the magnitude of the mass accretion rate and the size of the emitting region in images in optically thin synchrotron models, but optically thick models deviate markedly from this trend.

6.3 Phenomenological classification

For our fiducial semi-MAD simulation, upon exploration of parameter space, (f, β_c) models tend to outperform the jet-inspired Constant β_e and Bias (n) models with respect to spectral observations, and often outperform the detailed Electron Evolution Model with Turbulent Heating as well.

With respect to image morphology, observations favour compactness:

The images best satisfying the 86 GHz GMVA and 230 GHz EHT elliptical Gaussian size constraints for θ_{maj} are from the $(f, \beta_c) = (0.5, 1)$ model. It is noteworthy that this highest (f, β_c) pair producing the best spatial fit for the Critical Beta Electron Temperature Model also provides the best overall spectral fit, giving us indication that the image and spectral properties are correlated. Moreover, image compactness is related to image shape in our models, as the lowest $\beta_{e0} = 0.01$ providing the best (smallest) emitting region size for equipartition-inspired models has image morphology resembling the asymmetric crescent from the $(f, \beta_c) = (0.5, 1)$ model.

Upon a scan of model parameter space for our fiducial simulation, we find that images tend to aggregate into (at least) four broad categories, which are closely tied to spectra and related to variability as well:

(i) Thin, compact, asymmetric photon ring/crescent

This image morphology is exhibited for the Electron Evolution Model with Turbulent Heating and in parametrized models with high (f, β_c) , e.g. $\{(0.5, 0.1), (0.5, 1)\}$ or low β_{e0} , e.g. 0.01. The concomitant spectra are the best fit across our models, with the largest deviation coming from the $\beta_{e0} = 0.01$ Model's very flat spectrum in the IR band and mild X-ray excess. The mm-variability is characterized by light curves with moderate or high amplitude, oscillating rapidly on intra-hour scales – with the greater variability in the Constant β_{e0} branch breaking image degeneracy with (f, β_c) models.

(ii) Inflow–outflow boundary + thin photon ring

This image morphology is exhibited in models with $(f, \beta_c) \in \{(0.1, 0.01), (0.1, 0.1), (0.1, 1), (0.5, 0.01)\}$, and is accompanied by

the steepest spectra, sharply peaking near the IR bump. The radio variability is moderate amplitude and fast.

(iii) Thick photon torus

This image morphology is exhibited in the Constant β_e Model with $\beta_{e0} \in \{0.1, 1\}$, and the Bias Model with $n = 2$, and is accompanied by spectra with large X-ray excesses (and a flat overall spectrum for $\beta_{e0} = 0.1$). These models have low amplitude, slowly oscillating radio light curves.

(iv) Extended outflow

Occurring in the $n = 0$ Bias Model, this image morphology is linked to a flat overall spectrum with X-ray excess. This class is characterized by low amplitude, nearly monotonic radio variability within a day.

It is noteworthy that dominant image features are closely linked with dominant spectral features and tied to variability as well, and that these associations form the basis for distinct classes into which models governed by related physics – albeit different parametrizations thereof – can be identified.

6.3.1 SANE versus SEMI-MAD versus MAD simulation comparison

As we consider simulations outside of the fiducial simulation, new image morphologies emerge. For example, for the SANE simulation, the $(f, \beta_c) = (0.1, 1)$ Model has a distinctly helical outflow intensity map and a remarkably good spectral fit for all but the lowest frequencies (cf. Figs 11 and 12). Furthermore, it is notable that some of our models become similar to our favoured $(f, \beta_c) = (0.5, 1)$ Model in appropriate limits. In particular, as β_{e0} goes from 1 to 0.01 in the Constant β_e Model, intensity maps become more confined to small cylindrical radius and asymmetric for SANE, semi-MAD and MAD cases alike; and, for the MAD simulation, closer spectral fits are produced for the microwave, IR, and (especially) X-ray bands. The theoretical advancement of a single model unifying emission characteristics of accretion flow, corona, and outflow using a single simulation and small set of parameters would enable us to directly identify observed features with plasma and emission physics of different AGN components.

7 CONCLUSIONS AND FUTURE DIRECTIONS

We have used two simple classes of parametric emission prescriptions – the turbulent-heating-based Critical Beta Electron Temperature Model $T_e = f T_p e^{-\beta/\beta_c}$ and the equipartition-based Constant Electron Beta/Magnetic Bias Models $P_e = K_n P_B^n$, ($\beta_{e0} \equiv K_1$ for $n = 1$) – to explore a wide range of possible models for the images and spectra in the inner tens of gravitational radii around the supermassive black hole at the Galactic Centre. One of our models, $(f, \beta_c) = (0.5, 1)$, is observationally favoured for Sgr A* due to its agreement with respect to the spectrum, emitting region compactness and asymmetry. We stress that both observationally preferred images and spectra are associated with emission concentrated in a bright, crescent-shaped portion of the photon ring near the horizon, and that forthcoming EHT and GRAVITY data will further constrain our models.

It is worth noting that our intuitive one- and two-parameter models span new electron physics beyond what has been previously explored, and promise to bear upon AGN beyond Sgr A*. By surveying synthetic images and spectra in other parts of model parameter space, we may isolate the emission physics underlying

particular observational phenomena. We summarize these results as follows:

7.1 Images summary

Synthetic 230 GHz intensity maps on the scale of tens of gravitational radii appear:

- (i) Dominated by the inflow/outflow interface for the Critical Beta Electron Temperature Model
- (ii) More compact and asymmetric with increasing f or β_c
- (iii) Mixed with outflow/near-horizon photon ring emission for the Constant β_e and Bias Models
- (iv) More concentrated around horizon-circulating lensed disc emission for increasing β_{e0} and increasing n

7.2 Spectra summary

In comparison to the data, our parametrized synthetic $10^{11} \text{ Hz} < \nu < 10^{19} \text{ Hz}$ spectra have

- (i) More peaked slopes fairly consistent with the sub-mm bump but underproducing the low-frequency tail for the Critical Beta Electron Temperature Model
- (ii) Fairly consistent low-frequency slope but flatter peak and overproduction of low- and (especially) high-frequency emission for the Constant β_e Model
- (iii) Consistent low-frequency slope but broader peak and (in some cases vast) overproduction of high-frequency emission for the Bias Model

The steep radio spectra seen in the Electron Temperature Model is characteristic of emission from an adiabatically expanding coronal outflow, in which temperature rapidly declines in radius. The flatter radio spectra from the Constant β_e and Bias prescriptions are due to contributions from the highly magnetized outflow and the dependence of the latter emission functions exclusively on P_B . Although these latter models can explain many features of jets/outflows (including Sgr A*) such as Doppler beaming, knots and other magnetic field substructure, we have shown that they do not accurately describe the inner regions of discs/jets around Sgr A* (and perhaps, by analogy, other systems).

7.3 Future directions

Sgr A* viewed at 1.3 mm has exhibited intrahour variability (Johnson et al. 2015) in the inner $\sim 6r_g$ around a black hole whose Schwarzschild-radius-light-crossing-time is 40 s. In the future, it would be valuable to produce models with light curves in the simulations closely replicating the observational cadence and understand which range of models is most consistent with the observed variability. We may also add polarization maps to our pipeline to test whether electromagnetically dominated emission models in simulations with ordered magnetic field substructure, e.g. helical Blandford–Königl outflows, can help explain observations of a high degree of linear polarization in AGN cores.

The ‘observing’ simulations methodology is a key link between ever-advancing simulations and observations of the central engines of JAB systems. The EHT serves as a timely testbed for our emission models that aim to unite simulations and observations. The next works planned in this ‘Observing’ JAB simulations series are applications to the prominent jets in the giant elliptical galaxy M87 and the highly variable quasar 3C 279. Other EHT target

sources to be observed – and possibly, ‘observed’ – in the future include Cen A, NGC 1052, and OJ 287.

ACKNOWLEDGEMENTS

This work was supported in part by NSF grants AST 13-33612 and AST 1715054, *Chandra* theory grant TM7-18006X from the Smithsonian Institution, and a Simons Investigator award from the Simons Foundation. This work was made possible by computing time granted by UC Berkeley on the Savio cluster. RA carried out part of this work supported by the Alliance for Graduate Education and the Professorate (AGEP) and the Simons Foundation and the remainder of this work at the Black Hole Initiative at Harvard University, which is supported by a grant from the John Templeton Foundation. RA is also supported by the NSF MSIP grant no. AST-1440254. SR was supported in part by the NASA Earth and Space Science Fellowship and the Gordon and Betty Moore Foundation through grant no. GBMF7392 during part of the duration of this work. We all thank the scientific editor’s thorough and incisive comments, which greatly improved the overall quality of this work.

REFERENCES

Abuter R. et al., 2019, preprint ([arXiv:1904.05721](https://arxiv.org/abs/1904.05721))
 Anantua R., Blandford R., Tchekhovskoy A., 2018, *Galaxies*, 6, 31
 Anantua R., Emami R., Loeb A., 2019, preprint ([arXiv:1909.09230](https://arxiv.org/abs/1909.09230))
 Blandford R., Anantua R., 2017, *JPhCS*, 840, 012023
 Blandford R. D., Königl A., 1979, *ApJ*, 232, 34
 Blandford R. D., Znajek R. L., 1977, *MNRAS*, 179, 433
 Bower G. C. et al., 2015, *ApJ*, 802, 69
 Chael A., Rowan M., Narayan R., Johnson M., Sironi L., 2018, *MNRAS*, 478, 5209
 Chan C.-K., Psaltis D., Özel F., Narayan R., Sajdowski A., 2015, *ApJ*, 799, 1
 Davelaar J., Mościbrodzka M., Bronzwaer T., Falcke H., 2018, *A&A*, 612, A34
 Dexter J., Agol E., Fragile P. C., 2009, *ApJ*, 703, L142
 Dexter J., Agol E., Fragile P. C., McKinney J. C., 2010, *ApJ*, 717, 1092
 Doeleman S. S. et al., 2008, *Nature*, 455, 78
 Dolence J. C., Gammie C. F., Mościbrodzka M., Leung P. K., 2009, *ApJS*, 184, 387
 Event Horizon Telescope Collaboration et al., 2019, *ApJ*, 875, L1
 Falcke H., Markoff S., 2000, *A&A*, 362, 113
 Falcke H., Mannheim K., Biermann P. L., 1993, *A&A*, 278, L1
 Fishbone L. G., Moncrief V., 1976, *ApJ*, 207, 962
 Fish V. L. et al., 2011, *ApJ*, 727, L36
 Gammie C. F., McKinney J. C., Tóth G., 2003, *ApJ*, 589, 444
 Gillessen S. et al., 2010, *SPIE*, 7734, 77340Y
 Gillessen S. et al., 2017, *ApJ*, 837, 30
 Gold R., McKinney J. C., Johnson M. D., Doeleman S. S., 2017, *ApJ*, 837, 180
 Gravity Collaboration et al., 2018, *A&A*, 615, L15
 Howes G. G., 2010, *MNRAS*, 409, L104
 Issaoun S. et al., 2019, *ApJ*, 871, 30
 Johnson M. D. et al., 2015, *Science*, 350, 1242
 Johnson M. D. et al., 2018, *ApJ*, 865, 104
 Kataoka J., Sofue Y., Inoue Y., Akita M., Nakashima S., Totani T., 2018, *Galaxies*, 6, 27
 Lu R.-S. et al., 2018, *ApJ*, 859, 60
 Mahadevan R., Quataert E., 1997, *ApJ*, 490, 605
 Marrone D. P., 2006, PhD Thesis
 McKinney J. C., Gammie C. F., 2004, *ApJ*, 611, 977
 Mościbrodzka M., Falcke H., 2013, *A&A*, 559, L3

Mościbrodzka M., Gammie C. F., Dolence J. C., Shiokawa H., Leung P. K., 2009, *ApJ*, 706, 497

Mościbrodzka M., Falcke H., Shiokawa H., Gammie C. F., 2014, *A&A*, 570, A7

Neilsen J. et al., 2013, *ApJ*, 774, 42

Noble S. C., Leung P. K., Gammie C. F., Book L. G., 2007, *Class. Quantum Gravity*, 24, S259

Porth O., Olivares H., Mizuno Y., Younsi Z., Rezzolla L., Moscibrodzka M., Falcke H., Kramer M., 2017, *ComAC*, 4, 1

Ressler S. M., Tchekhovskoy A., Quataert E., Chandra M., Gammie C. F., 2015, *MNRAS*, 454, 1848

Ressler S. M., Tchekhovskoy A., Quataert E., Gammie C. F., 2017, *MNRAS*, 467, 3604

Ryan B. R., Ressler S. M., Dolence J. C., Gammie C., Quataert E., 2018, *ApJ*, 864, 126

Shcherbakov R. V., Penna R. F., McKinney J. C., 2012, *ApJ*, 755, 133

Sadowski A., Narayan R., McKinney J. C., Tchekhovskoy A., 2014, *MNRAS*, 439, 503

Sadowski A., Wielgus M., Narayan R., Abarca D., McKinney J. C., Chael A., 2017, *MNRAS*, 466, 705

Tchekhovskoy A., Narayan R., McKinney J. C., 2011, *MNRAS*, 418, L79

White C. J., Stone J. M., Gammie C. F., 2016, *ApJS*, 225, 22

Yuan F., Markoff S., Falcke H., 2002, *A&A*, 383, 854

Özel F., Psaltis D., Narayan R., 2000, *ApJ*, 541, 234

APPENDIX: TABLES

A1 Magnetic Bias Model normalization constant

For the Bias Model, the electron gas pressure P_e is prescribed to scale as powers n of the magnetic pressure P_B , requiring a magnetic-to-gas pressure conversion factor with units of pressure to power $1 - n$. Table A1 provides this factor by imposing a normalization condition in the semi-MAD simulation that the numerical average of P_B^2 equals that of $K_n P_B$ in the region between concentric cylindrical surfaces at $R = r_\rho = 1.89M$ and $R = 20M$, as well as $50M$ for comparison. An alternative normalization region in which the averaged is takeover annuli on the equatorial plane with the height

Table A1. Average values $\langle b^N \rangle$ from cylindrical radii $R = r_\rho = 1.87M$ to $R_{\max} \in \{20M, 50M\}$.

| N | Avg. out to $R_{\max} = 20M$ | Avg. out to $R_{\max} = 50M$ |
|-----|------------------------------|------------------------------|
| 1 | 0.0064 | 0.0023 |
| 2 | 0.00011 | 1.75e-05 |
| 3 | 5.52e-06 | 7.22e-07 |
| 4 | 4.63e-07 | 5.95e-08 |
| 5 | 4.57e-08 | 5.87e-09 |
| 6 | 4.89e-09 | 6.29e-10 |

of one simulation pixel produces similar results. Since the averages are similar for our different choices of region geometry and extent, we consider our normalization approach robust.

A2 Statistical analysis: moments

We may make quantitative our comparison of the disparate array of images generated from distinct physical processes by a comparison of statistical moments:

$$M_{n_1, n_2} = \sum_{i,j} x_i^{n_1} y_j^{n_2} I(x_i, y_j). \quad (A1)$$

First- and second-order image moments (centroid and gyroradius) for $-50M < x, y < 50M$ 230 GHz images in key models are presented in Table A2. The centroid of image intensity is right-offset, arising from asymmetric Doppler boosting of the accretion flow. However, it remains within the narrow-band between $5M < x < 10M$ and $-M < y < 3M$. The centroid right offset is consistent with the apparent mirror asymmetry in synthetic image brightness, especially in models producing a prominent bright-spot on the inner right edge of the disc. The higher moment gyroradius, including standard deviation, has greater variation across models due to contributions from larger radii emitting segments generated from low n or β_{e0} portions of Constant- β_e /Bias Model parameter space.

The image covariance matrices built from these moments are presented in Tables 2 and 3 in the main text.

Table A2. Images moment comparison of first and second moments for $-50M < x, y < 50M$ at 230 GHz for key models.

| Model | Centroid ($\frac{M_{10}}{M_{00}}, \frac{M_{01}}{M_{00}}$) | Radius of gyration ($\sqrt{\frac{M_{20}}{M_{00}}}, \sqrt{\frac{M_{02}}{M_{00}}}, \sqrt{\frac{M_{20}+M_{02}}{M_{00}}}$) |
|---|---|--|
| Electron Evolution with Turbulent Heating | ($6.56M, -0.15M$) | ($9.96M, 11.56M, 15.26M$) |
| Critical Beta Electron Temperature (f, β_c) | | |
| (0.1,0.01) | ($5.18M, 1.41M$) | ($11.76M, 20.58M, 23.70M$) |
| (0.1,0.1) | ($5.25M, 1.65M$) | ($10.70M, 16.92M, 20.02M$) |
| (0.1,1.0) | ($5.45M, 1.40M$) | ($10.39M, 14.31M, 17.69M$) |
| (0.5,0.01) | ($6.36M, 2.91M$) | ($11.51M, 18.80M, 22.04M$) |
| (0.5,0.1) | ($8.13M, 1.80M$) | ($10.81M, 10.53M, 15.09M$) |
| (0.5,1.0) | ($8.61M, 1.17M$) | ($10.78M, 7.93M, 13.38M$) |
| Constant Electron Beta (β_{e0}) | | |
| 0.01 | ($9.02M, 1.92M$) | ($16.44M, 21.41M, 26.99M$) |
| 0.1 | ($8.47M, -0.65M$) | ($24.51M, 22.55M, 33.31M$) |
| 1.0 | ($5.32M, 0.24M$) | ($27.32M, 23.24M, 35.86M$) |
| Magnetic Bias (n) | | |
| 0 | ($5.50M, -0.14M$) | ($26.44M, 30.05M, 40.02M$) |
| 1 | ($5.32M, 0.24M$) | ($27.31M, 23.24M, 35.86M$) |
| 2 | ($5.76M, -0.62M$) | ($26.85M, 22.86M, 35.26M$) |

Table A3. Pass-fail table of fiducial (edge-on, 230 GHz, semi-MAD simulation) models with respect to spectrum and all models for morphology (i.e. compactness/asymmetry measured by anisotropic Gaussian characteristic size θ_{maj}). Passing spectra intersect at least one data point in the frequency band considered. Failing spectra overproduce emission. F^* indicates models that underproduce emission in the IR or X-ray bands, where we expect non-thermal contributions neglected in our calculation to be important. For morphology, the simulations [SANE (S), semi-MAD (sM), and/or MAD (M)], observing angles and frequencies are specified for passing models.

| Model | Radio spectrum | NIR spectrum | X-ray spectrum | Morphology 86 GHz | Morphology 230 GHz |
|---|----------------|--------------|----------------|--|---------------------------|
| Electron Evolution with Turbulent Heating | P | P | <i>F</i> | <i>F</i> | <i>F</i> |
| Critical Beta Electron Temperature (f, β_c) | | | | | |
| (0.1, 0.01) | P | F^* | F^* | P ($S/0^\circ; M/0^\circ$) | <i>F</i> |
| (0.1, 0.1) | P | F^* | F^* | P ($S/0^\circ; M/0^\circ$) | <i>F</i> |
| (0.1, 1.0) | P | F^* | F^* | P ($S/0^\circ; M/0^\circ$) | <i>F</i> |
| (0.5, 0.01) | P | F^* | F^* | P ($S/0^\circ; M/0^\circ$) | <i>F</i> |
| (0.5, 0.1) | P | P | F^* | P ($S/0^\circ; M/0^\circ$) | <i>F</i> |
| (0.5, 1.0) | P | P | P | P ($S/0^\circ; S/90^\circ; M/0^\circ; M/90^\circ; sM/90^\circ$) | P ($S/90^\circ$) |
| Constant Electron Beta (β_{e0}) | | | | | |
| 0.01 | P | P | <i>F</i> | P ($M/0^\circ$) | <i>F</i> |
| 0.1 | P | P | <i>F</i> | P ($M/0^\circ$) | <i>F</i> |
| 1.0 | P | <i>F</i> | <i>F</i> | P ($M/0^\circ$) | <i>F</i> |
| Magnetic Bias (n) | | | | | |
| 0 | <i>F</i> | <i>F</i> | <i>F</i> | P ($M/0^\circ$) | <i>F</i> |
| 1 | P | <i>F</i> | <i>F</i> | P ($M/0^\circ$) | <i>F</i> |
| 2 | P | <i>F</i> | <i>F</i> | P ($M/0^\circ$) | <i>F</i> |

This paper has been typeset from a $\text{\TeX}/\text{\LaTeX}$ file prepared by the author.